Mechanism of structure formation in circular hydraulic jumps: numerical studies of strongly deformed free-surface shallow flows

Kenuke Yokoi [a,b,*], Feng Xiao [c]

[a] *Research Institute for Electronic Science and Division of Mathematics, Hokkaido University, Sapporo 060-0812, Japan*
[b] *Computer and Information Division, RIKEN (The Institute of Physical and Chemical Research), Wako 351-0198, Japan*
[c] *Department of Energy Sciences, Tokyo Institute of Technology, Yokohama 226-8502, Japan*

Abstract

We studied numerically circular hydraulic jumps of moderate Reynolds number to clarify the structure formation in circular hydraulic jumps. The numerical model has been constructed based on the CIP–CUP (cubic interpolated propagation–combined unified procedure) method, the level set method and the CSF (continuum surface force) model. The model can simulate strongly deformed interfaces as those found in hydraulic jump phenomena. In this study, we found that the pressure deviation from the hydrostatic equilibrium around the hydraulic jump is essential for the structure formation and that the surface tension plays an important role for the establishment of the pressure deviation. © 2002 Elsevier Science B.V. All rights reserved.

1. Introduction

A circular hydraulic jump is formed when a vertical liquid jet impinges on a horizontal surface and spreads out radially on the surface, which is easily observed in a kitchen sink. At the hydraulic jump, the height of the liquid surface suddenly varies and the flow also changes from a rapid (supercritical) flow to a slow (subcritical) flow. A picture of the circular hydraulic jump is shown in Fig. 1. The circular hydraulic jump is common in daily life and appears to be a simple phenomenon. However, it is much more complicated than it seems to be. In fact, it involves a strongly distorted free surface, a boundary layer and separation of flow. Studies concerning this phenomenon have been done by various approaches [1–14]. The circular hydraulic jump is relatively easily created in laboratory experiments, while the theoretical and numerical studies are limited by the complexities mentioned above.

In some experiments which have been performed by Ellegaard and coworkers [7], a more viscous liquid, ethylene-glycol, was used. Because of higher viscosity, a stable flow structure can develop in spite of the strongly deformed interface like Fig. 2(b). This simplifies theoretical and numerical treatments. If water is used, the turbulent

---

* Corresponding author.
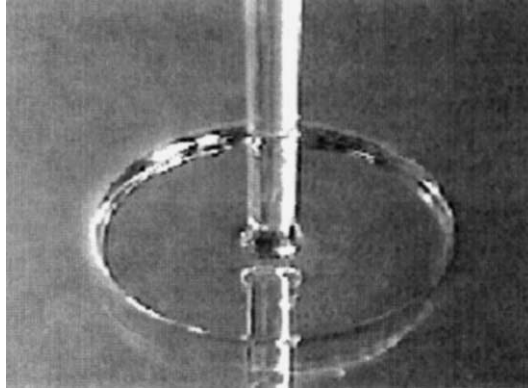*E-mail address:* kensuke@postman.riken.go.jp (K. Yokoi).

Fig. 1. Picture of a stationary circular hydraulic jump (photo: courtesy of C. Ellegaard). The fluid is ethylene-glycol.
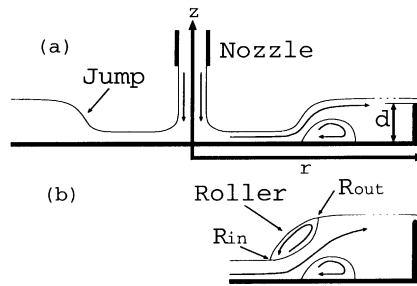

Fig. 2. Schematic figures of the experiment of the circular hydraulic jump. The radius of the wall is much larger than the radius of the jump. The flow from the nozzle is constant. (a) and (b) are called type I and type II, respectively. The points of the inside and outside of the roller are defined as (R_{in}^r, R_{in}^z) and (R_{out}^r, R_{out}^z).

effects arise especially for the case of Fig. 2(b) and the treatments become difficult. The depth on the outside of the jump can be controlled by varying the height of a circular wall d as shown in Fig. 2. The surface profiles for different wall heights in the experiments are shown in Fig. 3. The experimental results show that a circular hydraulic jump has two kinds of steady states which can be reached by changing d. When d is low or 0, a type I jump is formed as shown in Fig. 2(a). A type I jump contains an eddy on the bottom, called a 'separation bubble'. On increasing d, the jump becomes steeper until d reaches the critical d_c. If d becomes larger than d_c, the liquid outside of the
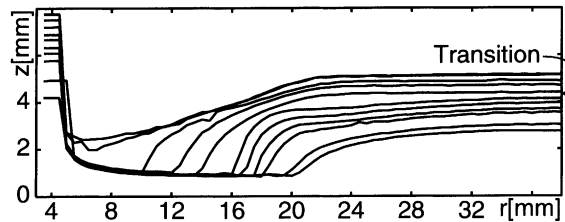

Fig. 3. Height profiles for various wall heights. A set of parameters, the density $\rho = 1110.0 \, \text{kg/m}^3$, the kinematic viscosity $\nu = 7.6 \times 10^{-6} \, \text{m}^2/\text{s}$, the surface tension coefficient $\sigma = 4.5 \times 10^{-2} \, \text{N/m}$, the volume flux $Q = 27 \, \text{ml/s}$ (Q is defined as $2\pi r \int_0^h u \, dz$ with h being the depth of the liquid), was used. The arrow shows that the transition from type I to type II flow occurs at a height of approximately 4 mm. (From [7].)

jump topples and another steady state, a type II jump, is formed as shown in Fig. 2(b). An eddy under the surface in a type II jump, the secondary circulation, which is usually called a 'roller', is observed. The existence of a roller distinguishes the two types of jumps.

In recent experiments of circular hydraulic jumps [10,11], it was found that various regular polygonal jumps can be developed from a circular hydraulic jump of a type II jump by controlling the height of the outer circular wall. As the wall height increases, the number of corners in the polygons decrease. Another kind of hydraulic jump, linear hydraulic jump, is formed in open channel flows and plays an important role for hydraulic engineering [3]. The linear hydraulic jump has flow structures and transitions, which are similar to those in circular hydraulic jumps. In the linear hydraulic jumps with the rollers, the excess energy of high velocity flows such as from sluice gates and spillways, is dissipated by the turbulent mixing around the roller. Actually, the hydraulic jumps prove to be useful for preventing the destruction of structures exposed to high velocity flows such as walls and bottoms of rivers. Hydraulic jumps appear also in pipe flows and coating flows, and play an important role for industrial topics such as cooling efficiency. It is widely recognized that hydraulic jump phenomena are important for the fields of fluid physics and engineering.

A simple and common theoretical approach to inviscid hydraulic jump problems, is due to Rayleigh [1]. In this approach, hydraulic jumps are regarded as a shock, a discontinuity, based on the analogy between the shallow water theory and gas theory [15]. Thus flow structure in the jump region is neglected. This approach has been widely used in hydraulic engineering. In a theoretical study of circular hydraulic jumps, a scaling relation of the radius of the circular hydraulic jump has been proposed [6]. This scaling relation is simple but agrees rather well with experimental data. A theoretical model for a type I jump has been developed by Bohr and coworkers [8,9,14] (see also Appendix A), but no model for the type II jump is available yet. In the theoretical model of Bohr et al., it is assumed that the pressure distribution is hydrostatic and that the surface tension force is negligible. However, those effects seem to play a crucial role in the formation of hydraulic jumps, especially in the type II state. The theoretical model is briefly reviewed and discussed in Appendix A.

Numerical simulations have been also performed for the circular hydraulic jump problems in [7], where a preset fixed boundary was used to represent the real free surface of the liquid. It should be noted that direct computation of the free surface of the liquid, which usually appears to be a very difficult problem, is important and essential to a numerical simulation of hydraulic jumps. In this paper, we perform numerical simulations which include the direct computation of the free surface using some advanced numerical algorithms. The full hydrodynamic equations including the effects of viscosity, gravity and surface tension are used. We have constructed a numerical model which avoids the explicit computation of boundary conditions across the interface and allows us to deal with a heavily distorted surface. By using the numerical model, we can avoid the complicated treatments of the free surface and are able to simulate directly the circular hydraulic jumps.

In this paper, we will report our numerical results on the mechanism of structure formation in circular hydraulic jumps by axisymmetric (r–z) simulations. Our results show that distinctive pressure fields are formed for a type I jump and a type II jump, respectively, and that these pressure fields play an important role for the transition of flow structure and its maintenance. The numerical model and the simulation configuration is discussed in Section 2. After the simulation results and discussions in Section 3, a short summary comes in Section 4. Most of the results presented in this paper have appeared earlier in a concise form [12,13].

2. Computational model and simulation configuration

The computational model is constructed on a rectangular fixed grid and based on the CIP–CUP (cubic interpolated propagation–combined unified procedure) method, the level set method and the CSF (continuum surface force) model

for the treatments of the free interfaces. The CIP–CUP method, developed by Yabe and Wang [16], is a solver of multi-phase flows, which treats both the liquid and gas in an unified framework. The level set method, constructed by Osher, Sethian and coworkers [20–22], is used to capture the moving surface and the surface tension is included via a CSF formulation by Brackbill et al. [23].

This numerical model can treat robustly liquid/gas multi-fluid flows with strongly deformed moving boundaries and surface tension, and are thus suitable for hydraulic jump simulations. We describe the main aspects of our numerical model in the following subsections.

2.1. Governing equations

We assume that both the liquid and gas are governed by the same governing equations but the physical parameters such as the density and viscosity coefficient are quite different. The governing equations can be written as

$$\frac{\partial \rho}{\partial t} + (\mathbf{u} \cdot \nabla)\rho = -\rho \nabla \cdot \mathbf{u}, \tag{1}$$

$$\frac{\partial \mathbf{u}}{\partial t} + (\mathbf{u} \cdot \nabla)\mathbf{u} = -\frac{\nabla p}{\rho} + \mathbf{g} + \frac{1}{\rho}\nabla \cdot \tau + \frac{\mathbf{F_{sv}}}{\rho}, \tag{2}$$

$$\frac{\partial e}{\partial t} + (\mathbf{u} \cdot \nabla)e = -\frac{p}{\rho}\nabla \cdot \mathbf{u}, \tag{3}$$

$$p = p(\rho, e), \tag{4}$$

where ρ is the density, $\mathbf{u}$ the velocity, p the pressure, $\mathbf{g}$ the gravitational acceleration, τ the viscous stress tensor, $\mathbf{F_{sv}}$ the surface tension force, and e the internal energy. Both the fluids are assumed to have an equation of state in the form of a polytropic gas, but with quite different sound speeds (a large sound speed for the liquid phase).

2.2. Solver of multi-phase flows

The set of the governing equations are solved by using the CIP–CUP method. In this method, a fractional step approach is used as follows:

$$f^{t+\Delta t} = \mathcal{A}^{\text{NA2}}(\mathcal{A}^{\text{NA1}}(\mathcal{A}^{\text{A}} f^t)). \tag{5}$$

Here f represents ρ, $\mathbf{u}$ and e, and $\mathcal{A}^{\text{A}}$, $\mathcal{A}^{\text{NA1}}$ and $\mathcal{A}^{\text{NA2}}$ represent the operators of difference schemes, respectively, for advection part, non-advection part 1 and non-advection part 2 defined as follows:

(1) advection part ($\mathcal{A}^{\text{A}}$):

$$\frac{\partial \rho}{\partial t} + (\mathbf{u} \cdot \nabla)\rho = 0, \tag{6}$$

$$\frac{\partial \mathbf{u}}{\partial t} + (\mathbf{u} \cdot \nabla)\mathbf{u} = 0, \tag{7}$$

$$\frac{\partial e}{\partial t} + (\mathbf{u} \cdot \nabla)e = 0, \tag{8}$$

(2) non-advection part 1 ($\mathcal{A}^{\text{NA1}}$):

$$\frac{\partial \mathbf{u}}{\partial t} = \mathbf{g} + \frac{1}{\rho}\nabla \cdot \tau + \frac{\mathbf{F_{sv}}}{\rho}. \tag{9}$$

(3) non-advection part 2 ($\mathcal{A}^{NA2}$):

$$\frac{\partial \rho}{\partial t} = -\rho \nabla \cdot \mathbf{u}, \tag{10}$$

$$\frac{\partial \mathbf{u}}{\partial t} = -\frac{\nabla p}{\rho}, \tag{11}$$

$$\frac{\partial e}{\partial t} = -\frac{p}{\rho} \nabla \cdot \mathbf{u}, \tag{12}$$

$$p = p(\rho, e). \tag{13}$$

The advection part and non-advection part 1 are computed by the CIP method [17,18] and the CUP method [16], respectively.

2.2.1. CIP method

The CIP method is a less-diffusive and stable algorithm to solve the advection equation

$$\frac{\partial f}{\partial t} + (\mathbf{u} \cdot \nabla) f = 0. \tag{14}$$

In one-dimensional case, the spatial profile between each neighboring cells of f is approximated with a cubic interpolation function

$$F_i(x) = a_i(x - x_i)^3 + b_i(x - x_i)^2 + f_i'(x - x_i) + f_i, \tag{15}$$

here f' is $\partial f / \partial x$. From the given f_i and f_i', the coefficients a_i, b_i can be determined by imposing the continuities of $F(x)$ and $(\partial F / \partial x)(x)$ between adjacent cells (see [17] for more detail). From $F_i(x)$, the time evolution of f can be calculated by shifting the interpolated function as

$$f_i^* = F_i(x_i - u_i \Delta t). \tag{16}$$

The time evolution of f' can be also calculated by a similar way. The interpolation function of f_i' can be obtained as the spatial derivative of F_i

$$F_i'(x) = \frac{\partial F_i(x)}{\partial x} = 3a_i(x - x_i)^2 + 2b_i(x - x_i) + f_i'. \tag{17}$$

The time evolution equation for f' is actually obtained by taking the spatial differentiation of (14) with respect to x,

$$\frac{\partial f'}{\partial t} + u\frac{\partial f'}{\partial x} = -f'\frac{\partial u}{\partial x}. \tag{18}$$

The fractional time step method is also applied for Eq. (18). The equation is separated to the advection part and non-advection part and it is calculated as

$$\frac{\partial f'}{\partial t} = -F_i'(x_i - u_i \Delta t)\frac{\partial u}{\partial x}. \tag{19}$$

This method can be extended easily to 2 and 3 spatial dimensions [18,19].

2.2.2. CUP method

The non-advection part 1 is solved with a finite difference method. To treat the multi-phase flows having various sound speeds, we use the CUP method which bases on a pressure Poisson equation.

The sound speed is defined as $C_s^2 = \partial p / \partial \rho$, hence a relation linking the pressure and the density reads as

$$\frac{\partial p}{\partial t} = C_s^2 \frac{\partial \rho}{\partial t}. \tag{20}$$

(10) and (20) give

$$\frac{\partial p}{\partial t} = -\rho C_s^2 \nabla \cdot \mathbf{u}. \tag{21}$$

(10), (11) and (21) are solved with a finite difference algorithm as

$$\frac{\rho^{t+\Delta t} - \rho^*}{\Delta t} = -\rho^* \nabla \cdot \mathbf{u}^{t+\Delta t}, \tag{22}$$

$$\frac{\mathbf{u}^{t+\Delta t} - \mathbf{u}^{**}}{\Delta t} = -\frac{\nabla p^{t+\Delta t}}{\rho^*}, \tag{23}$$

$$\frac{\mathbf{u}^{**} - \mathbf{u}^*}{\Delta t} = \mathbf{g} + \frac{1}{\rho^*} \nabla \cdot \tau^* + \frac{\mathbf{F}_{sv}}{\rho^*}, \tag{24}$$

$$\frac{p^{t+\Delta t} - p^*}{\Delta t} = -\rho^* C_s^2 \nabla \cdot \mathbf{u}^{t+\Delta t}, \tag{25}$$

where the superscript $*$ and $**$ mean the variables immediately after the calculations for the advection part and the non-advection part 1.

By substituting the divergence of (23) into (25), the Poisson equation of the pressure is obtained:

$$\nabla \cdot \left(\frac{\nabla p^{t+\Delta t}}{\rho^*} \right) = \frac{p^{t+\Delta t} - p^*}{\rho^* C_s^2 \Delta t^2} + \frac{\nabla \cdot \mathbf{u}^{**}}{\Delta t}, \tag{26}$$

where sound speed C_s depends on the physical properties of fluid such as p and ρ, and is calculated at each grid point. By solving the Poisson equation (26), the pressure for flows having various sound speeds can be calculated. $\mathbf{u}^{t+\Delta t}$ and $\rho^{t+\Delta t}$ then can be calculated from (22) and (23) by using $p^{t+\Delta t}$ calculated from (26).

2.3. Treatment of interface

The interface between the liquid and gas is captured by the level set method. The level set method has some important features that are required in the hydraulic jump calculations, for instance the method can handle topological changes in the evolving interface and the curvature of the front can be evaluated accurately [22].

The level set function is denoted as ψ, and satisfies

$$|\nabla \psi| = 1 \quad \text{for whole region}, \tag{27}$$

and

$$\psi(\mathbf{x}, t) \begin{cases} > 0 & \text{for the liquid}, \\ = 0 & \text{at the interface}, \\ < 0 & \text{for the gas}. \end{cases} \tag{28}$$

The function ψ is also called the distance function which represents the distance from the interface. The interface is represented by the zero-contour of ψ, called the zero-level set.

The time evolution of the level set function is calculated by the advection equation:

$$\frac{\partial \psi}{\partial t} + (\mathbf{u} \cdot \nabla)\psi = 0. \tag{29}$$

We used the CIP method to solve (29). However, after the advection calculation, the function does not appear in general to be a distance function. Therefore, to recover the feature of the distance function, the level set function must be re-initialized. The procedure is called re-initialization. Although there are some ways of re-initialization [22], in the present study, we used an iterative approach [21]. Re-initialization is done by solving the following problem to a steady state:

$$\frac{\partial \psi}{\partial \tau_t} = S(\psi)(1 - |\nabla \psi|), \tag{30}$$

where τ_t is an artificial time and $S(\psi)$ is the smoothed sign function:

$$S(\psi) = \frac{\psi}{\sqrt{\psi^2 + \varepsilon^2}}. \tag{31}$$

$S(\psi)$ is used to find out the zero-level set implicitly and becomes 0 at the zero-level set. The zero-level set thus does not move in the calculation of (30). At the position except the zero-level set, $S(\psi)$ has a non-zero value and the feature of $|\nabla \psi| = 1$ is recovered by (30). In our simulations, $\varepsilon = \Delta x (= \Delta y)$ was used.

The density (color) function ϕ which is used to define the physical properties for different materials such as viscosity and sound speed can be generated as a smoothed Heaviside function

$$\phi = H_\alpha(\psi), \tag{32}$$

with

$$H_\alpha(\psi) = \begin{cases} 0 & \text{if } \psi < -\alpha, \\ \frac{1}{2}\left[1 + \frac{\psi}{\alpha} + \frac{1}{\pi}\sin\left(\frac{\pi\psi}{\alpha}\right)\right] & \text{if } |\psi| \leq \alpha, \\ 1 & \text{if } \psi > \alpha, \end{cases} \tag{33}$$

where 2α represents the thickness of the transition region between the liquid phase and gas phase. In this time, $\alpha = (3/2)\Delta x$ was used. The density function is set as $\phi = 1$ for the liquid and $\phi = 0$ for gas.

2.4. Model of surface tension force

The surface tension force appears as the surface force

$$\mathbf{F_{sa}} = \sigma\kappa\mathbf{n}, \tag{34}$$

where σ is the fluid surface tension coefficient, κ the local mean curvature and $\mathbf{n}$ the outgoing unit vector normal to the interface. In this calculation, the surface tension force is modeled as a body force $\mathbf{F_{sv}}$ calculated by the gradient of the density function

$$\mathbf{F_{sv}} = \sigma\kappa\nabla\phi. \tag{35}$$

κ can be computed from

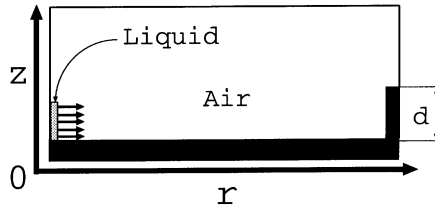$$\kappa = -(\nabla \cdot \mathbf{n}), \tag{36}$$

Fig. 4. Schematic figure of the configuration of the simulation.

and $\mathbf{n}$ is evaluated from the distance function in the level set method as follows:

$$\mathbf{n} = \frac{\nabla\psi}{|\nabla\psi|}. \tag{37}$$

Because the normal vector which is needed to calculate (36) can be directly computed from the distance function that is always well defined in the level set formulation, the curvature κ and thus the surface tension force can be computed accurately.

2.5. Configuration

In order to simulate a circular hydraulic jump, an axisymmetric model has been constructed. The configuration of the simulation model on an r–z plane is shown in Fig. 4. A no-slip condition was specified on the tank wall (as the dark bodies in Fig. 4). A horizontal inflow was put near the circular center as shown in Fig. 4. We made other boundary condition at the edge of calculation grid as an outflow condition. A rectangular staggered grid with $\Delta r = \Delta z = 0.1$ mm is used. [1] The time step Δt is determined from CFL conditions [21,24].

3. Simulation results and discussions

3.1. Validity of the computational model

As a validation of the present computational model, we compared the simulation results with the experimental observation [7] and the scaling relation [6]. Fig. 5 displays the comparison between the simulation and the experimental result. As the physical parameters of the simulation, the realistic parameters were used such as the density of liquid $\rho_l = 1110.0$ kg/m^3 and air $\rho_a = 1.2$ kg/m^3, the kinetic viscosity coefficient of liquid $\nu_l = 7.6 \times 10^{-6}$ m^2/s and air $\nu_a = 15.0 \times 10^{-6}$ m^2/s, the surface tension coefficient $\sigma = 4.5 \times 10^{-2}$ N/m, and the volume flux $Q = 27$ ml/s. It shows that the surface profile of the simulation agrees well with the experimental data. Fig. 6 shows the jump radius of the simulation results and the scaling relation:

$$r_j \sim q^{5/8} \nu^{-3/8} g^{-1/8}, \tag{38}$$

here $q = Q/2\pi$. In the present study, the jump is identified as the position where $\partial h/\partial r$ has its maximum. In Fig. 6, the jump radius is plotted against q (a) and the kinematic viscosity (b). Consistent with the scaling relation, the computational model gives a reasonable response to the different physical parameters. As expected from the scaling

---

[1] See [24] on how to implement the boundary conditions on the staggered grid. The staggered grid has been used widely in the MAC method type algorithms [24] and typical text books of computational fluid dynamics.
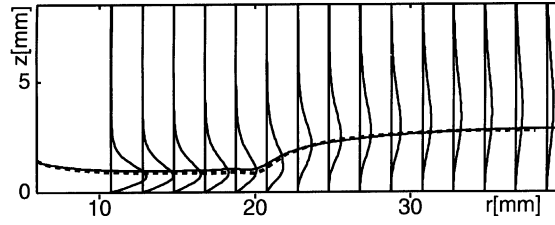
Fig. 5. The solid line represents the surface and the horizontal velocity profile of the numerical simulation. The dotted line shows the surface profile of the experiment (Fig. 3). The set of parameters in Fig. 3 is used. A 400×130 computational grid is used.
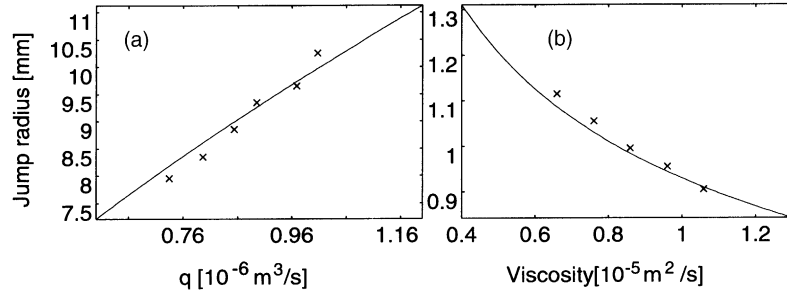

Fig. 6. The jump radii of the simulation results were plotted as a function of the volume flux (a) and the kinematic viscosity (b). The conditions as $d = 0$ mm was set for all cases. In (a), $\nu = 1.0 \times 10^{-5}$ m^2/s is used. $q = 0.9 \times 10^{-6}$ m^3/s is used for (b). Symbols and the solid line represent the jump radii of the simulation results and of the scaling relation.

relation, the jump radius becomes larger based on an $r_j \sim q^{5/8}$ law if the inflow flux is increased, while the jump radius becomes in an $r_j \sim \nu^{-3/8}$ law as the viscosity increases.

3.2. Surface profiles and pressure distributions in steady states

Simulations were carried out with different heights of the outer circular wall d. The volume flux of the inflow is $Q = 5.6$ ml/s and the viscosity of the liquid is $\nu_l = 7.6 \times 10^{-6}$ m^2/s. Steady surface profiles for various wall heights are shown in Fig. 7. The three lower profiles are type I jumps, and the two upper profiles are type II jumps. We observe that the jump becomes steeper as the wall height increases for a type I jump, while for a type II, the slope of the jump appears less steep than that of type I with a high wall height. These are consistent with the experimental results in Fig. 3.

The pressure distributions after eliminating the hydrostatic effect (referred to as the dynamic pressure distribution) around the jump of the steady state for the various wall heights in Fig. 7 are shown in Fig. 8. For the cases of type I
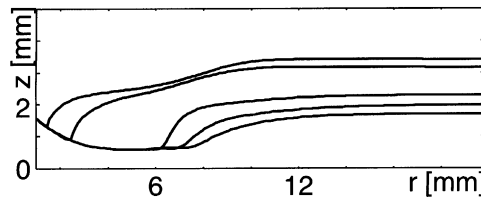

Fig. 7. Surface profiles for different wall heights d. $Q = 5.6$ ml/s and $\nu_l = 7.6 \times 10^{-6}$ m^2/s are used.
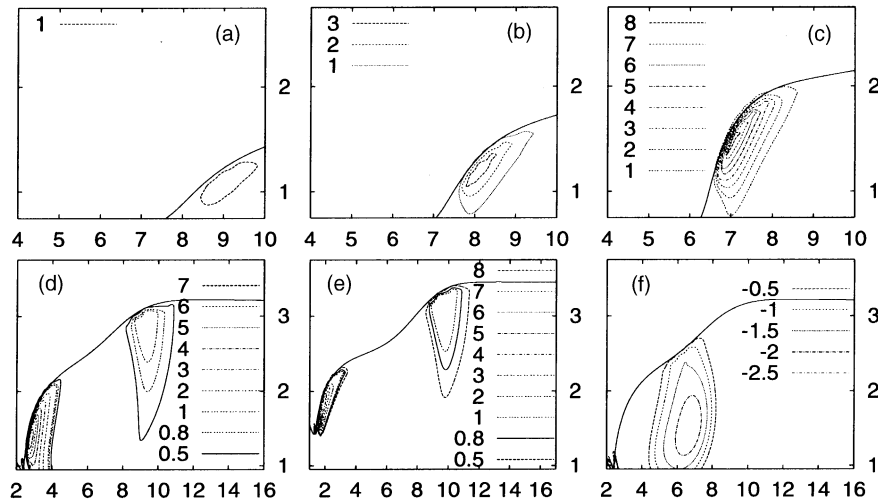
Fig. 8. (a)–(e) Dynamic pressure (Pa) contours around the jump for over 0 Pa from the lowest profile in Fig. 7. (f) Dynamic pressure contour of the fourth profile for under 0 Pa.

(Fig. 8(a)–(c)), a high pressure region (referred to hereafter as the primary high pressure) dominating a wide region under the jump surface is observed. In a type II jump, two high pressure regions are developed around the inner side of the jump (referred to as the primary high pressure) and the outer side of the jump (referred to as the secondary high pressure) as shown in Fig. 8(d) and (e) and the relatively low pressure area is formed between the two highs and corresponds to the location of a roller (Fig. 8(f)). It is observed that the pressure distributions for the type I and the type II jumps are quite different.

Here, we consider the causes of the formation of these pressure fields. In the type I jumps (Fig. 8(a)–(c)), for higher wall height d, the curvature of the interface immediately after the jump becomes larger, then the surface tension is strengthened, because the surface tension force is proportional to the curvature. In order to counteract this surface tension and keep the jump surface steady, a larger rise in pressure is required. In the type II jumps (Fig. 8(d) and (e)), the liquid surface appears convexly curved around the secondary high pressure region or the outer edge of the roller. This curve of the free surface around the outer edge of the roller is also observed in experiment as shown in Fig. 3. To counteract the surface tension caused by this curved surface, the secondary high pressure must be required to keep a steady surface like the type I jump. From this argument, we may conclude that the formation of the high pressure regions strongly depends on the surface tension force. Moreover, in the case of type II, the low pressure region is formed in the roller region (Fig. 8(f)). This pressure field is required to counteract the centrifugal force produced by the circulation in the roller.

We also examined the relationships among the surface tension force, the pressure gradient force and the viscous force around the jump. Fig. 9 shows the accelerations produced by these three forces. From Fig. 9, it can be seen that the pressure gradient force caused by the dynamic pressure is the main force balancing the surface tension force, while the viscous force is almost negligible. Here it should be noted that all the forces are balanced if the inertial force is also included.

3.3. Transition from type I jump to type II jump

We investigated the transition process from a type I jump to a type II jump to study the mechanism. We started the simulation from the steady state of a type I jump (the second profile after the lowest in Fig. 7). The time of this
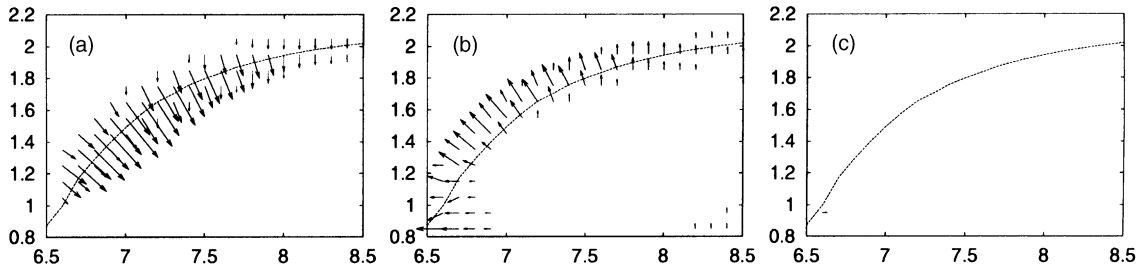
Fig. 9. The figures show accelerations caused by the surface tension force (a), the pressure gradient force (b) and the viscous force (c) around the jump in a type I steady jump (the third profile in Fig. 7).

initial state was set as $t = 0$ s. We simulated until the steady state of a type II jump (the fourth profile in Fig. 7) was reached by suddenly increasing the wall height at $t = 0$ s.

Fig. 10 shows the time evolution of the surface profile and the horizontal velocity profile. Fig. 11 also represents the time evolution of the surface. As time increases, the jump becomes steeper until around $t = 2.352$ s. At that time, it breaks, reverse flow is formed beneath the surface and the slope of the jump becomes gentle. Finally, the flow state approaches the steady state of the type II jump. The roller is thus a consequence of a steepened jump, and its occurrence leads to a gentler jump.

Fig. 12 represents the time evolution of the dynamic pressure distributions. As time increases and the jump becomes steeper, and the high pressure becomes stronger until the transition. Immediately before the transition, the high pressure region spreads out and the strength becomes slightly weaker. After the transition, the high pressure region is split and a secondary high pressure region is created. It is expected that the dynamic pressure plays an important role for the transition.
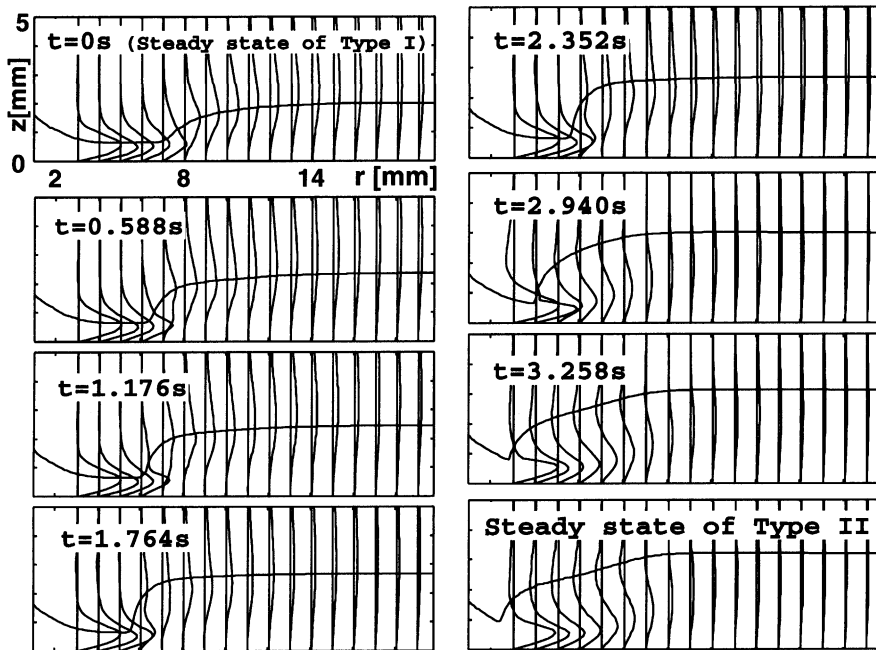

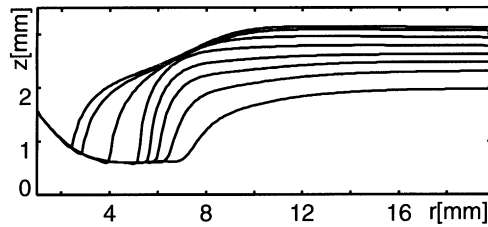Fig. 10. The time evolution from a type I jump to a type II jump at 0.588 s intervals.

Fig. 11. The time evolution from a type I jump to a type II jump. The lowest one is the initial state.

Based on the results of Fig. 12, we can discuss the reason for the transition from a type I jump to a type II jump. In a type I jump, a primary high pressure region is formed and a pressure gradient which tends to cause a reverse flow along the surface is formed beneath the surface, as shown in Fig. 13. Approaching to the transition, the primary high pressure becomes stronger and pressure gradient also becomes larger. When the pressure gradient force from the primary high pressure (F_p in Fig. 13) becomes stronger than the driving force from the main flow (F_m in Fig. 13), a roller is created. The competition between the pressure gradient force (F_p) and the driving force from the main flow (F_m) determines the occurrence of the roller.
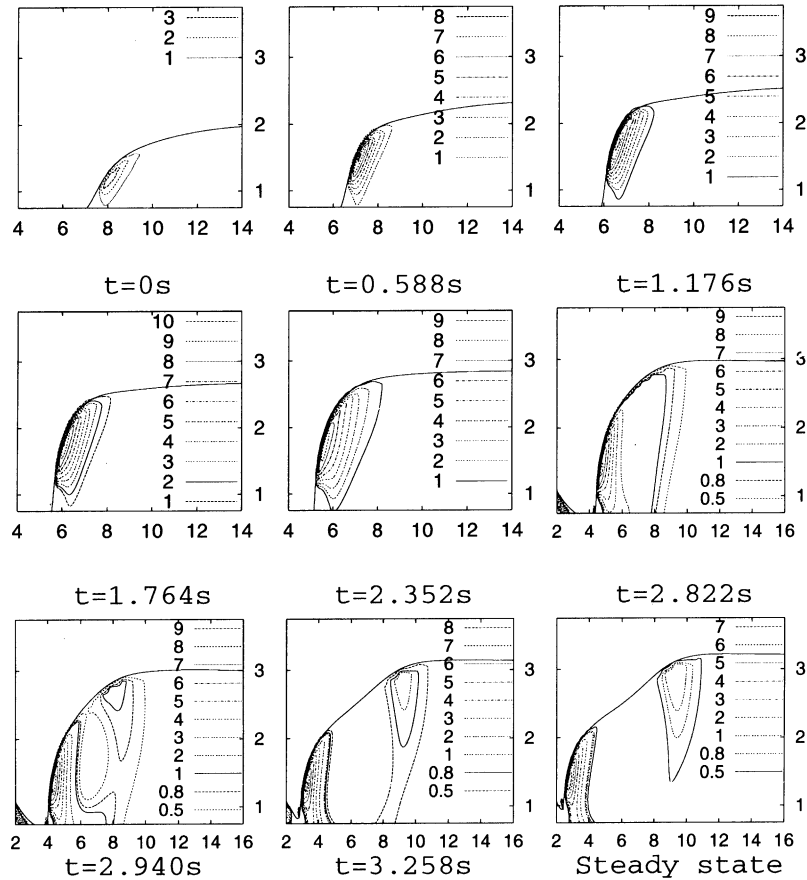
Fig. 12. The time evolution of the dynamic pressure distributions (Pa) around the jump.
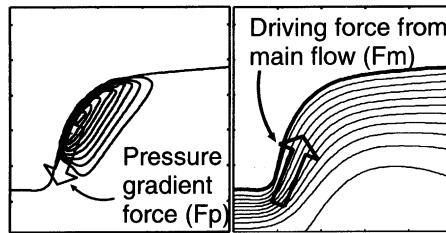
Fig. 13. A schematic figure shows a role of the pressure field for the transition from a type I jump to a type II jump. Left and right figures show the dynamic pressure distribution and the streamline, respectively, in the type I jump.
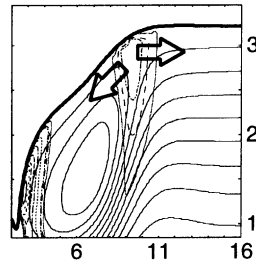

Fig. 14. The figure shows the streamline, the dynamic pressure distribution and the surface profile of the fourth profile in Fig. 7. The arrows represent the pressure gradient force to separate the flow by the secondary high pressure.

3.4. Relationships between roller and pressure distributions

The pressure distribution plays an important role for the creation and the maintenance of the roller. We observe that the high pressure on the outer side of the jump (the secondary high pressure) coincides with the separation point of the flow, as shown in Fig. 14. This secondary high pressure continuously provides a pressure gradient force to separate the flow and to maintain the upper reverse flow for the roller. The reverse flow from the separation point moves down along the jump surface until it meets another high pressure (the primary high pressure) on the upstream side of the jump. The fluid motion is decelerated when it approaches the high pressure on the inner side of the jump. The direction of motion is then changed, and joins the main stream again around the confluent point R_{in}.

We further simulated the disappearance process of a roller (the transition process from a type II jump to a type I jump) to study the details of the relation between the pressure field and the roller. We started from the steady state of a type II jump (the fourth profile from the lowest in Fig. 7). Its surface profile is shown as the topmost one in Fig. 15. The time of this initial state was set $t = 0$. We simulated until the steady state of a type I jump (the second
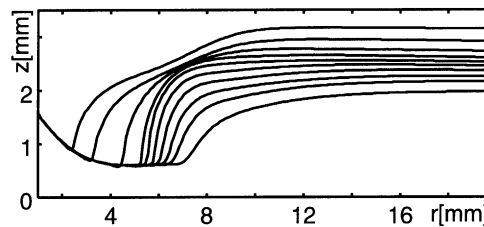

Fig. 15. The time evolution of the surface profile from the type II jump to the type I jump. The topmost profile is the initial state.
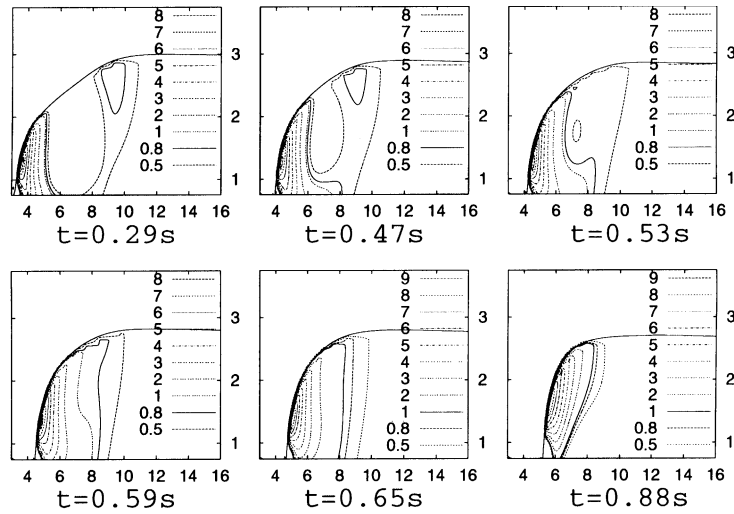
Fig. 16. The time evolution of the dynamic pressure distribution in the transition from a type II jump to a type I jump. Fig. 8(d) and (b) correspond to $t = 0$ and the final steady state.

profile in Fig. 7) was reached by lowering the wall height at $t = 0$. Fig. 15 displays the surface profiles at different instants. The flow underwent a transition from a type II jump to a type I jump. The evolution of the dynamic pressure field and the maximum value of the secondary high pressure are shown in Figs. 16 and 17, respectively. The initial pressure distribution is characterized by two high pressure regions and a roller. As time increases, the secondary high pressure becomes weaker, and finally vanishes around 0.55 s. It appears that the reduction of the secondary high pressure is associated with the decline in the curvature of the surface around the secondary high pressure. Meanwhile, the primary high pressure does not experience any significant change and finally turns out to be the primary high pressure in the type I jump. In order to give a quantitative measure for the roller, we calculated the horizontal width of the roller as $R_{out}^r - R_{in}^r$. Fig. 18 shows the time evolution of the roller width. With the secondary high pressure abating, the roller width decreased. This process was significantly enhanced after the secondary high pressure completely disappeared (from 0.55 s) because the pressure gradient becomes exactly opposite to the reverse flow of the roller. Around 0.75 s, the roller disappeared. With the secondary high pressure and the roller having abated, the fluid eventually approached the steady state of a type I jump.
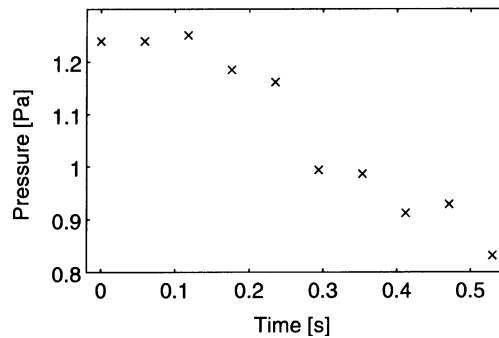

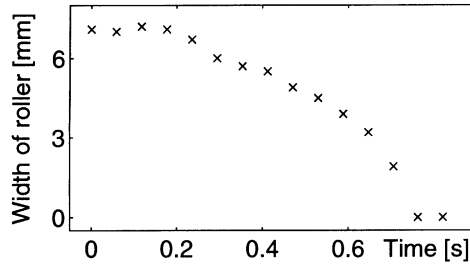Fig. 17. The time evolution of the maximum value of the secondary high pressure.

Fig. 18. The time evolution of the width of the roller.

4. Conclusions

Axisymmetrical simulations were carried out for the circular hydraulic jump with a strongly deformed free surfaces by using a model including direct computation of the interface and surface tension force. We reproduced numerically the type I jump and the type II jump that have been experimentally observed. The transitions between these two types hydraulic jumps were also investigated.

From the numerical results, we found that the pressure increase beneath the jump surface plays an important role in generating the reverse flows, which are needed for the occurrence and the maintenance of the roller. A correlation between the pressure field and the surface tension force is also observed. The establishment of the pressure distribution around a jump can be explained as a consequence of the balance of various forces and thus a roller is created under a proper pressure pattern.

Acknowledgements

Appendix A. Approach by integral model

Here, we briefly explain a reduced model for the circular hydraulic jump, which can deal with a flow structure in a type I jump [8,9,14]. The model is based on the Kármán–Pohlhausen method to treat the boundary layer.

The governing equations for the circular hydraulic jump in a stationary and radially symmetric state were written

$$u_r + \frac{u}{r} + w_z = 0, \tag{A.1}$$

$$uu_r + wu_z = -\frac{p_r}{\rho} + \nu \left(u_{rr} + \frac{u_r}{r} - \frac{u}{r^2} + u_{zz} \right), \tag{A.2}$$

$$uw_r + ww_z = -\frac{p_z}{\rho} - g + \nu \left(w_{rr} + \frac{w_r}{r} + w_{zz} \right), \tag{A.3}$$

where u and w are the radial and vertical components of the velocity, ρ the density, p the pressure and ν the kinetic viscosity coefficient. The subscripts r and z denote the partial derivatives. The no-slip boundary condition is imposed on the bottom:

$$u(r, 0) = w(r, 0) = 0. \tag{A.4}$$

The dynamic boundary conditions on the free surface $z = h(r)$ are

$$p - \frac{2\rho\nu}{1 + h_r^2}\{h_r^2 u_r + w_z - h_r(w_r + u_z)\} = 0, \tag{A.5}$$

$$\nu\{(1 - h_r^2)(w_r + u_z) - 2h_r(u_r + w_z)\} = 0, \tag{A.6}$$

where the surface tension force has been neglected. In the incompressible stationary flow, the volume flux Q:

$$r \int_0^h u \, \mathrm{d}z = \text{const.} = \frac{Q}{2\pi} = q, \tag{A.7}$$

must be constant.

The horizontal and vertical lengths and velocities are rescaled as follows:

$$r_* = (q^5 \nu^{-3} g^{-1})^{1/8} \simeq 3.0 \, \text{cm}, \tag{A.8}$$

$$z_* = (q\nu g^{-1})^{1/4} \simeq 0.15 \, \text{cm}, \tag{A.9}$$

$$u_* = (q\nu g^3)^{1/8} \simeq 12 \, \text{cm/s}, \tag{A.10}$$

$$w_* = (q^{-1}\nu^3 g)^{1/4} \simeq 0.7 \, \text{cm/s}, \tag{A.11}$$

respectively [6], where typical experimental parameters $\nu \simeq 0.1 \, \text{cm}^2/\text{s}$ and $Q \simeq 30 \, \text{cm}^3/\text{s}$ are used. The typical radial scale r_* and velocity u_* are much larger than vertical scale z_* and velocity w_*. Then the set of the governing equations can be reduced with $O(\epsilon^2)$ error here $\epsilon = z_*/r_*$. The reduced governing equations and boundary conditions, rewritten in the dimensionless form are as follows:

$$uu_r + wu_z = -p_r + u_{zz}, \tag{A.12}$$

$$0 = -p_z - 1, \tag{A.13}$$

$$p(r, h) = 0, \tag{A.14}$$

$$u_{z|z=h} = 0. \tag{A.15}$$

From (A.13) and (A.14), the hydrostatic pressure distribution is obtained

$$p(r, z) = h(r) - z. \tag{A.16}$$

By substituting (A.16) to (A.12),

$$uu_r + wu_z = -h' + u_{zz}, \tag{A.17}$$

is obtained, here the prime is the derivative with respect to r. The equation is solved with the continue equation (or mass conservation equation) (A.1), the boundary conditions (A.4) and (A.15), and the flux conservation condition (A.7) of dimensionless form:

$$r \int_0^h u \, \mathrm{d}z = 1. \tag{A.18}$$

By integrating (A.17) and (A.18) over z from 0 to h and using (A.1) and the boundary condition, the averaged momentum equation:

$$v(F_2 v)' = -h' - \frac{1}{h} u_z(r, 0), \tag{A.19}$$

can be obtained. Here

$$v(r) = \frac{1}{h} \int_0^h u(r, z)\, dz, \tag{A.20}$$

$$F_2 = \frac{1}{h} \int_0^h \left(\frac{u}{v}\right)^2 dz, \tag{A.21}$$

v is the averaged velocity. The flux conservation condition is transferred to

$$vhr = 1. \tag{A.22}$$

The velocity profile is approximated as the third order polynomial: [2]

$$u(r, z) = v(r)(a_1(r)\eta + a_2(r)\eta^2 + a_3(r)\eta^3), \tag{A.23}$$

where $\eta = z/h(r)$. The parameters a_1, a_2, a_3 are reduced to just one; $\lambda(r)$ by implementing the flux conservation condition (A.22) and the boundary condition (A.15) as follows:

$$a_1 = \lambda + 3, \qquad a_2 = -\tfrac{1}{2}(5\lambda + 3), \qquad a_3 = \tfrac{4}{3}\lambda. \tag{A.24}$$

Then, (A.19) is transferred to

$$v(F_2(\lambda)v)' = -h' - (\lambda + 3)\frac{v}{h^2}, \tag{A.25}$$

where

$$F_2(\lambda) = \frac{6}{5} - \frac{\lambda}{15} + \frac{\lambda^2}{105}. \tag{A.26}$$

Here, the unknown variables are three, v, h and λ, however the equations are two, (A.25) and (A.22). To close the system, one more equation is needed. The equation can be obtained using an approach of Kármán–Pohlhausen type, that (A.17) is at $z = 0$:

$$h' = u_{zz|z=0}. \tag{A.27}$$

It is transferred to

$$h' = -(5\lambda + 3)\frac{v}{h^2}. \tag{A.28}$$

Finally, by substituting $v = 1/rh$ into (A.25) and (A.28),

$$\frac{dF_2}{d\lambda}\lambda' = \frac{4r\lambda}{h} + F_2 \frac{h^4 - (5\lambda + 3)}{rh^4}, \tag{A.29}$$

$$h' = -\frac{5\lambda + 3}{rh^3}, \tag{A.30}$$

can be obtained. The equations are solved by imposing two boundary conditions, two surface points $h_1(r_1)$ and $h_2(r_2)$ read from experimental data, by the shooting method, because the velocity profile λ is unknown. The model can reproduce a type I jump, the stationary circular hydraulic jump including the separation bubble, quite accurately.

---

[2] For the case of parabolic profile, see [2,6].

However, the model has two problems for the representation of a type II jump. The first point is the assumption of the hydrostatic pressure distribution (A.16). In the assumption, it is difficult to know the reason of the reverse flow formation along the surface, which appears in the transition from a type I jump to type II jump and in the roller. The transition may be explained from the pressure gradient to produce the reverse flow, which is formed by the height difference of the surface, slope of the jump, like the eddy on the bottom. But it has not been confirmed. On the other hand, for the formation of the reverse flow in the roller, we cannot think of the reason of the reverse flow generation in the assumption. The second point is that the velocity profile has been approximated as the cubic polynomial (A.23). In the case of type II, that the roller is on the separation bubble as shown in Fig. 2(b), it seems that the velocity profile of the biquadratic (fourth-order) polynomial must be used. However, in our sense, it is awfully difficult to construct the model using the biquadratic velocity profile.

References

 [1] L. Rayleigh, Proc. Roy. Soc. London A 90 (1914) 324.
 [2] I. Tani, J. Phys. Soc. Jpn. 4 (1949) 212.
 [3] V.T. Chow, Open Channel Hydraulic, McGraw-Hill, New York, 1959.
 [4] E.J. Watson, J. Fluid Mech. 20 (1964) 481.
 [5] A.D.D. Craik, R.C. Latham, M.J. Fawkes, P.W.F. Gribbon, J. Fluid Mech. 112 (1981) 347.
 [6] T. Bohr, P. Dimon, V. Putkaradze, J. Fluid Mech. 254 (1993) 635.
 [7] T. Bohr, C. Ellegaard, A.E. Hansen, A. Haaning, Physica B 228 (1996) 1.
 [8] T. Bohr, V. Putkaradze, S. Watanabe, Phys. Rev. Lett. 79 (1997) 1038.
 [9] V. Putkaradze, Ph.D. Thesis, Niels Bohr Institute, University of Copenhagen, 1997.
[10] C. Ellegaard, A.E. Hansen, A. Haaning, K. Hansen, A. Marcussen, T. Bohr, J.L. Hansen, S. Watanabe, Nature 392 (1998) 767.
[11] C. Ellegaard, A.E. Hansen, A. Haaning, K. Hansen, A. Marcussen, T. Bohr, J.L. Hansen, S. Watanabe, Nonlinearity 12 (1999) 1.
[12] K. Yokoi, F. Xiao, Phys. Lett. A 257 (1999) 153.
[13] K. Yokoi, F. Xiao, Phys. Rev. E 61 (2000) R1016.
[14] S. Watanabe, V. Putkaradze, T. Bohr, Preprint, physics/0008219 (2000).
[15] L.D. Landau, E.M. Lifshitz, Fluid Dynamics, Pergamon Press, Oxford, 1987.
[16] T. Yabe, P.Y. Wang, J. Phys. Soc. Jpn. 60 (1991) 2105.
[17] T. Yabe, T. Aoki, Comput. Phys. Commun. 66 (1991) 219.
[18] T. Yabe, et al., Comput. Phys. Commun. 66 (1991) 233.
[19] T. Aoki, CFD J. 4 (1995) 279.
[20] S. Osher, J.A. Sethian, J. Comput. Phys. 79 (1988) 12.
[21] M. Sussman, P. Smereka, S. Osher, J. Comput. Phys. 114 (1994) 146.
[22] J.A. Sethian, Level Set Methods and Fast Marching Methods, Cambridge University Press, Cambridge, 1999.
[23] J.U. Brackbill, D.B. Kothe, C. Zemach, J. Comput. Phys. 100 (1992) 335.
[24] F.H. Harlow, J.E. Welch, Phys. Fluids 8 (1965) 2182.